Relaxation processes and high-field coherent spin manipulation in color center ensembles in 6*H*-SiC

Victor A. Soltamov,[1] Boris V. Yavkin,[2] Andrey N. Anisimov ⓘ,[1,*] Harpreet Singh ⓘ,[3] Anna P. Bundakova,[1]
Georgy V. Mamin,[2] Sergei B. Orlinskii,[2] Evgeniy N. Mokhov,[1] Dieter Suter ⓘ,[3] and Pavel G. Baranov[1]

[1]*Ioffe Institute, Politekhnicheskaya 26, 194021 St. Petersburg, Russia*
[2]*Federal Center of Shared Facilities of Kazan State University, 420008 Kazan, Russia*
[3]*Fakultat Physik, Technische Universitat Dortmund, D-44221 Dortmund, Germany*

Coherent spin manipulations of spin-$\frac{3}{2}$ color center ensembles in 6*H*-SiC crystal have been studied in high magnetic fields using methods of pulsed electron paramagnetic resonance, Rabi oscillations, and pulsed electron-electron double resonance under optical alignment conditions of the spin level populations. Rabi oscillation experiments show room temperature coherent control of these spin-$\frac{3}{2}$ color center ensembles in strong magnetic fields. A sharp decrease of the spin-lattice relaxation time T_1, $\sim$40 times, was observed in 6*H*-SiC at magnetic field of $\sim$3.5 T with increasing temperature from 100 to 300 K, while the spin-spin relaxation time T_2 is only shortened by $\sim$1.3 times. With an increase in the magnetic field, the times T_1 and T_2 were shown to decrease. The relaxation time T_1 in the case of magnetic field directed along the axis of the spin-$\frac{3}{2}$ center is $\sim$2 times longer than T_1 in magnetic field perpendicular to this axis. Relaxation times of the spin center in crystal grown with a reduced concentration of an isotope ^{29}Si are significantly longer than crystal, with the natural content of isotopes. With a decrease in the ^{29}Si content in our experiments by a factor of $\sim$5, the effective nuclear spin bath in SiC is reduced by a factor of $\sim$2. In a zero magnetic field resonance, transitions are allowed as magnetic dipole transitions with frequency ω_0 which correspond to the zero-field splitting. In zero magnetic field and in fixed magnetic fields, the Rabi frequency was shown, using so-called "Feynman-Vernon-Hellwarth transformation," to be $\omega_R = |\gamma| B_1$. In pulsed electron-electron double resonance experiments, a change in the intensity of the electron spin echo signal corresponding to one of the spin-allowed fine structure transitions is recorded depending on the sweep of the second frequency. The experiments show the possibility to coherently detect the optical spin alignment between $M_S = \pm\frac{3}{2}$ via optically pumped silent $M_S = \pm\frac{1}{2}$ sublevels of the spin-$\frac{3}{2}$ color centers, including a detection of Rabi oscillations.

I. INTRODUCTION

In recent years, silicon carbide (SiC) has attracted continuously growing interest as a technologically prospective platform for spintronics [1–14] with an ability for single-spin engineering and control [15–20]. Demonstrated spin properties of the color centers open avenues for quantum sensing and quantum computing. The optically induced population inversion of spin states leads to stimulated microwave emission, which can be used to implement solid-state masers and extraordinarily sensitive radiofrequency amplifiers. Electron spins of the defect center in SiC are excellent candidates for quantum information processing and future spin-based quantum devices.

One of the challenges in quantum information science is to achieve long spin coherence time (T_2) for spin color centers in SiC. We will consider vacancy-related color centers characterized by the ground and excited spin states with $S = \frac{3}{2}$ (so-called "spin-$\frac{3}{2}$ center"). The spin-$\frac{3}{2}$ centers in 6*H*-SiC are designated as the corresponding zero-phonon lines (ZPLs): V1, V2, and V3. The absorption and photoluminescence (PL)

spectra of V1, V2, and V3 spin-$\frac{3}{2}$ centers in SiC represent the series of ZPLs accompanied by the sideband phonon replicas. The number of ZPLs corresponds to the number of nonequivalent positions in the lattice.

The electron paramagnetic resonance (EPR) spectra can be fitted by a standard spin Hamiltonian for $S = \frac{3}{2}$:

$$H = g\mu_B \mathbf{B} \cdot \mathbf{S} + D\left[S_Z^2 - \frac{S(S+1)}{3} \right], \qquad (1)$$

where the first and second terms correspond to the Zeeman interaction and fine structure splitting, respectively, μ_B is the Bohr magneton, and g is the electron g factor. Without an external magnetic field ($B = 0$), the ground state (GS) is split due to the presence of the axial crystal field with fine-structure parameter D. For $S = \frac{3}{2}$ spin state, the zero-field splitting (ZFS) between $M_S = \pm\frac{1}{2}$ and $M_S = \pm\frac{3}{2}$ sublevels $\Delta = 2|D|$. The EPR angular dependencies show that all the centers are oriented along the c axis of the hexagonal 6*H*-SiC polytype.

Previously, the main studies of relaxation processes in spin-$\frac{3}{2}$ centers were performed on 4*H*-SiC crystals [21] and only on one type of center, the V2 center. Nevertheless, from a fundamental point of view, studies of spin-$\frac{3}{2}$ centers in 6*H*-SiC crystals are of particular interest. We note the main reasons for

*aan0100@gmail.com

the importance of such studies. (i) There are several spin-$\frac{3}{2}$ centers, V1, V2, and V3, with a difference in the ZFS: for V1 and V3 centers, $\Delta = 28$ MHz; for the V2 center, $\Delta = 128$ MHz. (ii) The sign of D for the V2 center is positive, while for V1/V3 centers, the sign of D is negative [22], which determines the opposite order of arrangement of the energy spin levels for these centers. (iii) There are significant differences in the order of alignment of the populations of spin levels for these centers. (iv) For V1/V3 centers, the nature of alignment depends on temperature; moreover, at a temperature of $\sim$30 K, level populations equalize, and the EPR [electron spin echo (ESE)] signal disappears.

Isotope engineering is often used to suppress the relaxation mechanism caused by interactions with nuclear spins. The electron spin coherence time T_2 is inversely proportional to the concentration of nuclear spins [17]. Two types of nuclear spins, ^{13}C and ^{29}Si with natural abundance $\rho_{C13} = 1.1\%$ and $\rho_{Si29} = 4.7\%$, respectively, contribute to the decoherence of spin centers. The electron spin decoherence in an applied magnetic field B is caused by the magnetic fluctuations from many nuclear spins. The decoherence mechanisms and a longer coherence time in SiC were shown through numerical calculations [23] to be a consequence of the suppression of the heteronuclear spin pair flip-flop process. The suppression of heteronuclear spin crosstalk can be achieved by applying a strong magnetic field. Spin decoherence in strong magnetic fields is mainly caused by flip-flop of nuclear spin pairs. It was shown in Ref. [23] that, different from the homonuclear spin pair cases (^{13}C-^{13}C and ^{29}Si-^{29}Si pairs), the heteronuclear spin pair flip-flop (i.e., ^{29}Si-^{13}C) is significantly suppressed in strong fields, which is the key point for understanding the longer T_2 time of defect centers in SiC. For heteronuclear spin pairs, the splitting also consists of the Zeeman frequency difference due to the different gyromagnetic ratios γ for ^{13}C and ^{29}Si.

The electron spin relaxation times of spin-$\frac{3}{2}$ centers in SiC in different magnetic fields will be investigated. It will be confirmed that spin centers in SiC are considerable candidates for quantum information processing and future spin-based quantum devices.

II. EXPERIMENTAL

All results reported here are obtained using three types of 6*H*-SiC crystals with a natural content of isotopes and enriched in ^{28}Si isotope. We used neutron and electron irradiation to generate silicon-vacancy (V_{Si})-related spin-$\frac{3}{2}$ color centers.

(i) A crystal of 6*H*-SiC polytypes (sample #1) was grown by the sublimation technique with nitrogen donor concentration of the order of 5×10^{16} cm^{-3} (it was estimated by EPR before the irradiation). It contains a natural abundance of ^{29}Si (4.7%) and ^{13}C (1.1%) nuclear spins ($I = \frac{1}{2}$). The crystal has been irradiated with neutrons with energies of 3–5 MeV and neutron fluence $\Phi n = 10^{16}$ cm^{-2}. Typical concentration of V_{Si}-related spin-$\frac{3}{2}$ color centers was $\sim$10^{15} cm^{-3}.

(ii) A 6*H*-^{28}SiC crystal (sample #2) was grown by the sublimation technique with nitrogen donor concentration of the order of 5×10^{16} cm^{-3}. A content of the ^{28}Si isotope with

a zero nuclear magnetic moment increased up to $\sim$99% (the natural content of ^{28}Si is 92.2%). A content of the ^{29}Si isotope having a nonzero magnetic moment was $\sim$0.9%. The information was obtained by simulating EPR spectra with hyperfine (HF) interactions with 12 silicon atoms located in the second shell relative to the silicon vacancy. The crystal was irradiated with 2 MeV electrons. The concentration of spin-$\frac{3}{2}$ color centers in the sample was estimated as $\sim$3.2 $\times$ 10^{14} spins/cm^3 by comparison with an EPR signal of the test sample. As a result, the average distance between paramagnetic centers is estimated at $\sim$150 nm.

(iii) A commercial 6*H*-SiC wafer (sample #3) with a natural content of isotopes with nitrogen donor concentration $<1 \times 10^{17}$ cm^{-3} was irradiated with 2 MeV electrons. The concentration of spin-$\frac{3}{2}$ color centers in the sample was estimated as $\sim$1 $\times$ 10^{14} spins/cm^3 (see Supplemental Material [24]).

To study relaxation processes, we used the methods of pulsed EPR at frequencies of 95 GHz (W band) and 9.5 GHz (X band) and pulsed electron-electron double resonance (PELDOR) at a frequency of 9.5 GHz. The ESE technique was used for measurements of a spin-lattice (T_1) and spin-spin (T_2) relaxation times of spin-$\frac{3}{2}$ color centers in silicon carbide. The measurements were carried out on an ELEXSYS pulse-EPR spectrometer 580/680 Bruker operating in two frequency ranges (9.5 and 95 GHz) in stationary and pulsed modes at temperatures of 5–300 K.

Rabi oscillation measurements were performed in a pulse-EPR spectrometer working at the X band. The static magnetic field has always been chosen to correspond to the middle of the EPR line. A microwave pulse starts at $t = 0$ and coherently drives the magnetization. At the end of the pulse, the magnetization is recorded. Because of the dead time of the spectrometer ($\sim$80 ns), it is impossible to directly measure the magnetization right after the pulse. Two methods for the detection were used. The first one is simply to record the free induction decay (FID) emitted by the system when the microwave field is shut down; the second method used the ESE technique.

A diode laser operating at 785 and/or 808 nm was used to excite all types of spin-$\frac{3}{2}$ color centers through phonon-assisted absorption at low and room temperature (RT). In some experiments, we used irradiation by two lasers simultaneously with different wavelengths to increase the optical pump power through phonon-assisted absorption of several spin centers.

III. RESULTS

A. Electron spin-lattice relaxation time T_1 and spin-spin relaxation time T_2

Spin-lattice relaxation time T_1 and spin-spin relaxation time T_2 were measured in two frequency ranges: the X band (9.5 GHz) and the W band (95 GHz) at different temperatures under conditions of optical alignment of the spin level populations. We first measure the spin-lattice relaxation time T_1, which determines the absolute limit for spin coherence. To measure T_1 the ESE signal intensity was monitored by applying inversion-recovery pulse sequence π-ΔT-$\pi/2$-τ-π,
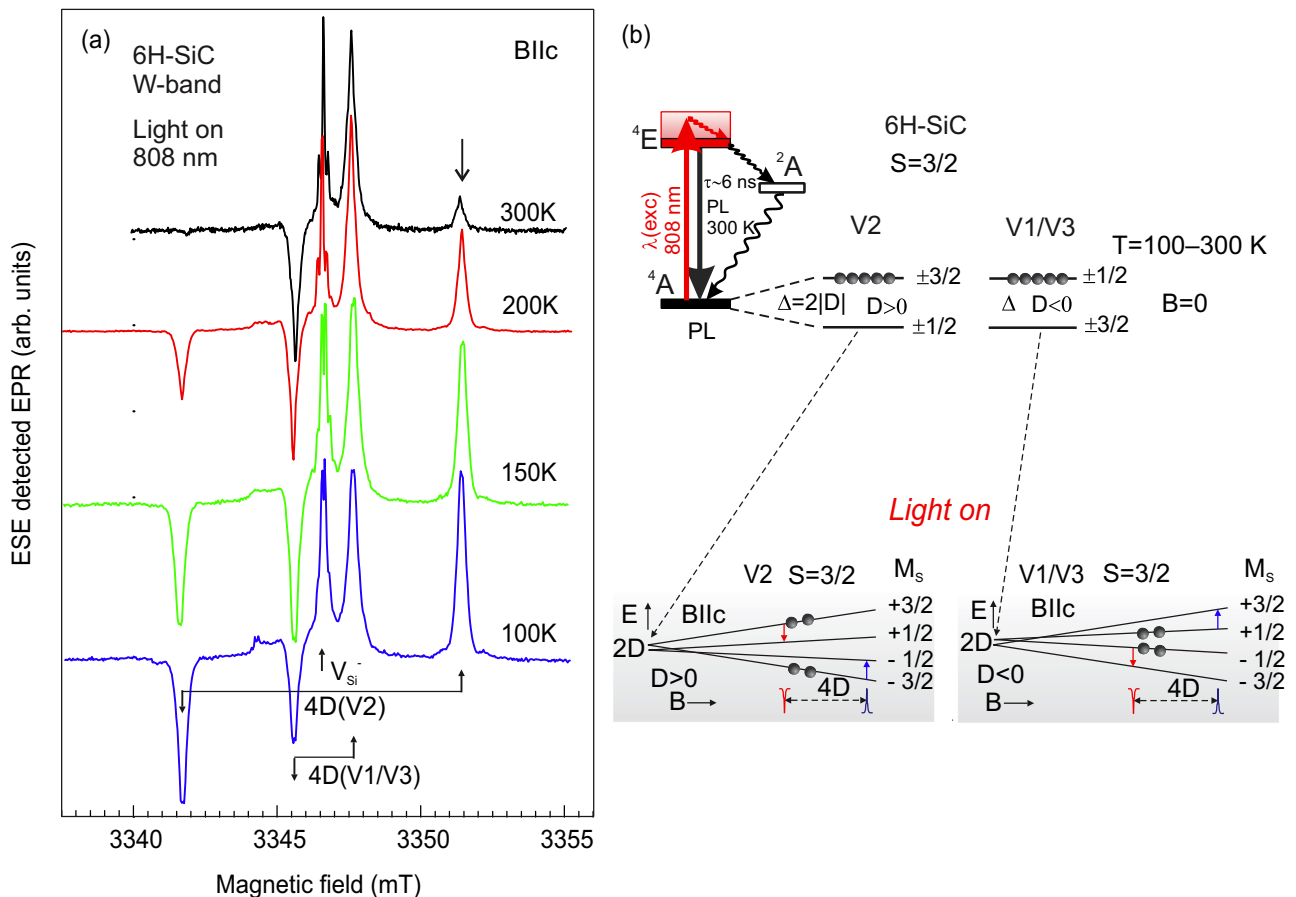
FIG. 1. (a) Electron spin echo (ESE) detected electron paramagnetic resonance (EPR) spectra of spin-$\frac{3}{2}$ color centers under 785/808 nm optical excitation in the neutron-irradiated 6*H*-SiC crystal (sample #1), orientation $B \parallel c$, temperatures of 300, 200, 150, and 100 K. The optical excitation results in inverse populations of the spin levels and to a phase inversion for certain transitions. (b) The schemes of optically induced alignment of spin level populations in zero magnetic field at room temperature (RT) for the V2 and V1/V3 spin-$\frac{3}{2}$ centers in 6*H*-SiC crystals (top). Energy level diagrams for V2 and V1/V3 centers according to Eq. (1) and light-induced inverse population of the spin levels in magnetic field at RT (bottom). Optical transitions (absorption and emission) are represented in the optical excitation-emission cycle by solid lines, nonradiative transitions by wavy lines.

where ΔT was varied from 900 ns up to the desired value (5 to 10 T_1 value, i.e., ~1 ms) and τ was kept at 200 ns. The first pulse creates a nonequilibrium population. The Hahn echo generated by the second and third pulses monitors the recovery to the thermal equilibrium population. Here, T_2 measurements were done using Hahn echo decay sequence $\pi/2$-τ-π, where τ was incremented from 200 ns up to 40 μs by equal steps of 40 ns each. The values of T_1 and T_2 were obtained from the fits of the measured ESE decay curves by $y = B \times [1 - \exp(-\Delta T/T_1)]$ and $y = A \times \exp(-2\tau/T_2)$, respectively.

B. Spin-$\frac{3}{2}$ color centers in neutron irradiated 6*H*-SiC crystal

Figure 1(a) shows ESE-detected EPR spectra of spin-$\frac{3}{2}$ centers in neutron irradiated 6*H*-SiC crystal (sample #1) in the *W* band (95 GHz). The spectra were measured at different temperatures of 300, 200, 150, and 100 K under 808 nm optical excitation and magnetic field orientation along the *c* axis. Optical excitation leads to an inverse population of the spin levels and, as a result, to phase inversion for certain

transitions. EPR signals of the three types of spin-$\frac{3}{2}$ color centers, V1, V3, and V2, are observed. The ZFS for the V1 and V3 centers $2|D| = 28$ MHz and coincides within the experimental error; ZFS for the V2 center of $2|D| = 128$ MHz. In the central part of the spectra, one can see the EPR line of a negatively charged silicon vacancy V_{Si}^- located in a regular defect-free environment (see, e. g., Ref. [19]).

The schemes of optically induced alignment of populations of spin levels in a zero magnetic field for the V2 and V1/V3 spin-$\frac{3}{2}$ centers in 6*H*-SiC crystals are shown at the top of Fig. 1(b). There is an inverse population of spin levels in a zero magnetic field (maser effect) at RT. Energy level diagrams for V2 and V1/V3 centers according to Eq. (1) and light-induced inverse population of the spin levels in the magnetic field at RT are shown at the bottom of Fig. 1(b). At zero magnetic field, $M_S = \pm\frac{1}{2}$ and $\pm\frac{3}{2}$ sublevels of the GS ^{4}A split (ZFS). Under illumination, inverse population in the GS is created due to the nonradiative spin-selective decay via the ^{2}A metastable state. Optical transitions (absorption into sideband phonon replicas and emission) are represented in the optical excitation-emission cycle by solid lines, nonradiative
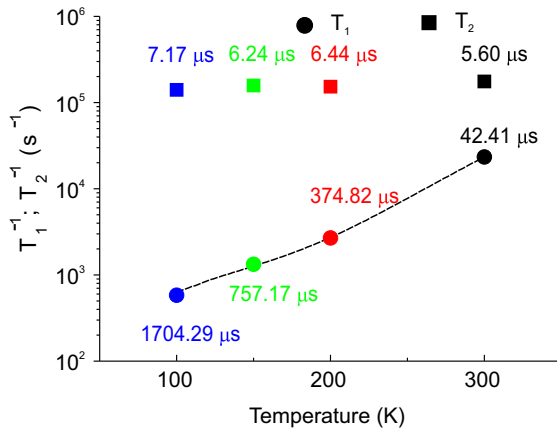
FIG. 2. Relaxation times T_1 and T_2 (as the rate $1/T_1$ and $1/T_2$) measured at different temperatures in the *W* band (95 GHz) from the high-field component of V2 centers, which corresponds to transition $M_S = -\frac{3}{2} \rightarrow -\frac{1}{2}$, indicated by the arrow in Fig. 1(a). Dashed line is a guide for the eyes.

transitions by wavy lines. Lifetime in the excited state ^{4}E, τ, is of ~6 ns.

Figure 2 shows the relaxation times T_1 and T_2 (as the rate $1/T_1$ and $1/T_2$) measured in the *W* band on the high-field component of the V2 centers, which corresponds to transition $M_S = -\frac{3}{2} \rightarrow -\frac{1}{2}$ [indicated by the arrow in Fig. 1(a)] at different temperatures. Dashed line is a guide for eyes.

An increase in temperature from 100 to 300 K leads to a sharp decrease in the time T_1, ~40 times, from 1.7 ms to 42 μs, while the time T_2 is shortened by ~1.3 times, from 7.2 to 5.6 μs; that is, it can be argued that it is almost independent of temperature. It should be noted that neutron irradiation leads to the creation of many defects, of various types, which in any case create additional relaxation mechanisms, that is, lead to a shortening of relaxation times T_1 and T_2.

Figure 3 shows the ESE-detected EPR spectra measured at RT. The upper spectrum is ESE-detected EPR recorded in the *W* band; the bottom spectrum is the same measured in the *X* band. Values of the measured T_1 and T_2 relaxation times are indicated for corresponding transitions of V1/V3 and V2 spin centers. The measurements were provided on the low-field and high-field EPR transition ($M_S = \pm\frac{1}{2} \leftrightarrow \pm\frac{3}{2}$) of each center under 785 nm light illumination and magnetic field applied parallel to the *c* axis.

A trend of the changes for times T_1 and T_2 in different magnetic fields is visible in Fig. 3: an increase of the magnetic field (when moving from the *X* to the *W* range) results in a decrease of the times T_1 and T_2, while at the same time, when moving from V2 to V1/V3, there is a multidirectional change in the times T_1 and T_2 : T_1 lengthens, and T_2 shortens.

An analysis of the experimental results for T_1 and T_2, presented in Fig. 3 and Table I, gives grounds to draw several conclusions of interest for applications. A tenfold increase in the magnetic field leads to a comparatively insignificant decrease in the relaxation times by <2 times. The ratio between T_1 and T_2 ranges from 10 to 20. Time T_1 increases with the transition from center V2 to centers V1/V3, while time T_2 changes in the opposite direction. Nevertheless, the
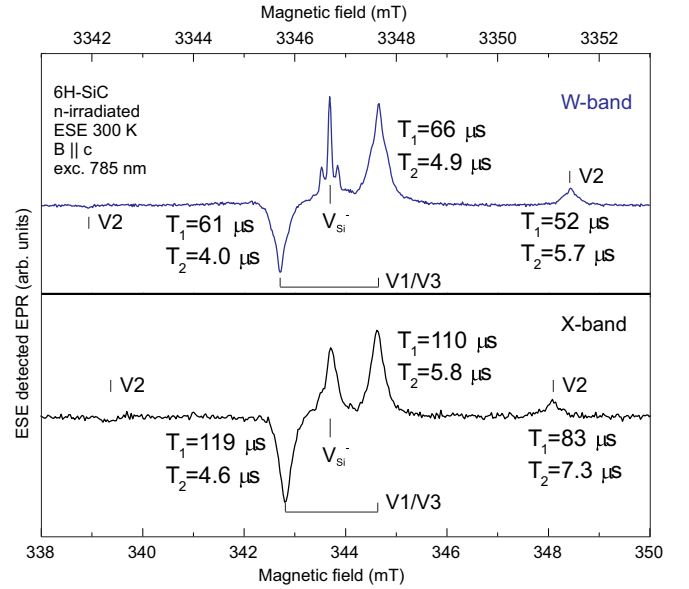

FIG. 3. Room-temperature electron spin echo (ESE)-detected electron paramagnetic resonance (EPR) spectra of spin-$\frac{3}{2}$ color centers in sample #1 under 785 nm optical excitation $B \parallel c$. The upper figure shows the ESE spectra recorded in the *W* band; the bottom figure is the same measured in the *X* band. Values of the measured T_1 and T_2 relaxation times are indicated for corresponding transitions of V1/V3 and V2 spin-$\frac{3}{2}$ centers. A slight difference in the splitting of the fine structure in the *X* and *W* bands is due to the inaccuracy of setting the orientation $B \parallel c$.

relaxation times of optically aligned spin sublevels, measured at RT, are long enough for quantum operations in the system. Thus, the measurements have unambiguously showed that the spin color centers based on V_{Si} are the closest competitors to the negatively charged nitrogen vacancy center (NV center) in diamond.

It seems appropriate to compare these values with the relaxation times T_1 and T_2 in a zero magnetic field. In our previous work, we studied RT relaxation times T_1 and T_2 of the spin-$\frac{3}{2}$ ensemble in 6*H*-SiC during free precession as well as under the influence of different refocusing schemes [25]. From the fit, the RT T_1 relaxation time for the V1/V3 centers is 142.1 ± 3.6 μs and for the V2 centers 107 ± 6.6 μs.

The resulting values for T_2 were 3.73 ± 0.13 μs and 3.31 ± 0.24 μs for the V1/V3 and V2 centers, respectively [25]. It can be seen that the relaxation times T_1 and T_2 obtained in zero magnetic field at RT [25] are comparable with the

TABLE I. RT relaxation times T_1 and T_2 in 6*H*-SiC crystal irradiated with neutrons (sample #1), $B \parallel c$, under light excitation 785 nm. A low intensity of the V2 low-field signal did not make it possible to reliably measure the relaxation times.

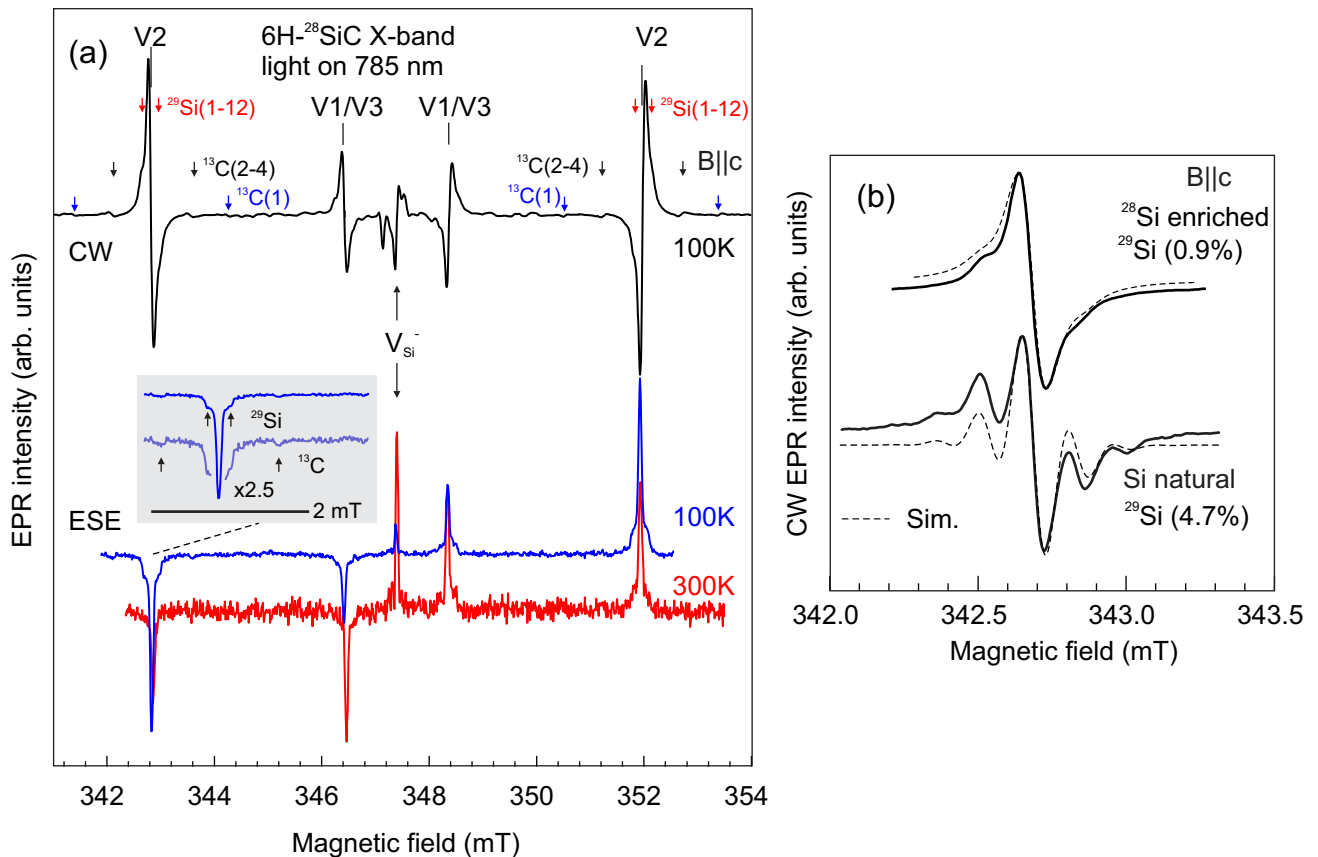| Line	T_1, *X* band	T_2, *X* band	T_1, *W* band	T_2, *W* band
V2 high field	83 μs	7.3 μs	52 μs	5.7 μs
V2 low field	–	–	–	–
V1/V3 high field	110 μs	5.8 μs	66 μs	4.9 μs
V1/V3 low field	119 μs	4.6 μs	61 μs	4.0 μs

FIG. 4. (a) The continuous wave (CW) X band electron paramagnetic resonance (EPR) spectra (top line) and electron spin echo (ESE) detected EPR spectra (bottom) of spin-$\frac{3}{2}$ color centers in a $6H$-^{28}SiC crystal (sample #2) measured in orientation of the magnetic field $B \parallel c$ under optical excitation of 785 nm, which leads to phase inversion for certain transitions. V2 and V1/V3 centers are indicated. Hyperfine (HF) interactions with the nearest neighbor four carbon atoms (C_{NN}) and the next nearest neighbor 12 silicon atoms (Si_{NNN}) relative to the silicon vacancy. The inset shows the low-field line of V2 centers, with the decoding of HF interactions with C_{NN} carbon atoms and Si_{NNN} silicon atoms. (b) Comparison of the EPR signals recorded in a $6H$-SiC crystal with natural ^{29}Si isotope content and in a $6H$-SiC crystal with depleted ^{29}Si isotope content; solid line is experiment, modulation amplitude was of 0.05 G; dashed line is simulation.

corresponding times recorded in strong magnetic fields (see Figs. 1–3).

Multiple refocusing pulses can extend the lifetime of the coherence further by more than an order of magnitude compared with the case of a single ESE. The lifetimes of the coherence for multiple pulses are 56 ± 11 μs and 51 ± 4 μs for the V1/V3 and V2 centers, respectively [25].

C. Spin-$\frac{3}{2}$ color centers in electron-irradiated $6H$-^{28}SiC crystal

Figure 4(a) shows continuous wave (CW) X band EPR spectra (top line) and ESE-detected EPR spectra (bottom) of spin-$\frac{3}{2}$ color centers in a $6H$-^{28}SiC crystal (sample #2) measured in the orientation of the magnetic field parallel to the c axis of the crystal, $B \parallel c$, under 785 nm optical excitation; V2 and V1/V3 centers are indicated. The optical excitation leads to phase inversion; the energy level diagrams for V2 and V1/V3 centers and the light-induced inverse population of the spin levels are the same as previously shown in Fig. 1(b). HF interactions with the nearest neighbor four carbon atoms (C_{NN}) of the first coordination sphere and the next nearest neighbor 12 silicon atoms (Si_{NNN}) of the second sphere relative to the silicon

vacancy are indicated by arrows. The inset shows the low-field line of the V2 centers, with the decoding of HF interactions with C_{NN} carbon atoms and Si_{NNN} silicon atoms.

Two types of HF interactions were directly observed in the EPR spectra [Fig. 4(a)]. The first type of HF interaction occurs with the ^{13}C nucleus located in the nearest neighbor shell to the V_{Si}^{-} site. They are strongly anisotropic and reflect the tetrahedral symmetry of the nuclear spin locations. Figure 4(a) displays also almost isotropic HF structure for the Si_{NNN} atoms with respect to the negatively charged silicon vacancy V_{Si}^{-}. Here, $^{13}C_1$ denotes the interaction with the carbon atom oriented along the c axis, and $^{13}C_{2-4}$ denotes the interactions with atoms located in the basal plane with the bonds inclined by the angle $\vartheta = 71°$ relative to the c axis.

To confirm the isotopic composition of the crystal, i.e., the decrease in the concentration of the isotope with the nuclear magnetic moment, we compared the HF structure of the two samples. Figure 4(b) shows a comparison of the EPR signals recorded in a $6H$-SiC crystal with natural ^{29}Si isotope content and in a $6H$-SiC crystal with depleted ^{29}Si isotope content; solid line indicates the experiment; modulation amplitude was 0.05 G; dashed line indicates the simulation. HF interaction with ^{29}Si nucleus for 12 Si_{NNN} atoms in the next nearest

TABLE II. Spin-lattice relaxation time T_1 of spin-$\frac{3}{2}$ centers measured in a $6H$-^{28}SiC crystal (sample #2). The empty cells in the table correspond to the low intensity of the EPR signals, which did not make it possible to reliably measure the relaxation times.

Line	T_1, $B \parallel c$, 100 K	T_1, $B \perp c$, 100 K	T_1, $B \parallel c$, 300 K
V2 high field	6.7(1) ms	3.7 ms	0.1 ms
V2 low field	7.0(2) ms	3.4 ms	–
V1/V3 high field	5.2(2) ms	3.3 ms	0.15 ms
V1/V3 low field	6.2(4) ms	–	–

neighbor shell of Si vacancy is well resolved. It is immediately evident that the line of the V2 center for an ^{28}Si isotopically enriched sample and a sample with a natural abundance of nuclei is different. The satellites belonging to the interaction with Si$_{NNN}$ atoms sharply decrease in intensity in a $6H$-SiC crystal with depleted ^{29}Si isotope content. The width of the individual lines remains practically unchanged. This is because the width of these individual lines is mainly determined by a rather strong HF interaction with ^{13}C nuclei in the third coordination sphere. This interaction, as follows from our electron nuclear double resonance (ENDOR) research, is about several Gauss. Note that, in sample #2, isotope content of ^{13}C (1.1%) and ^{29}Si (0.9%) is approximately the same. Thus, the general EPR line can be substantially narrowed by changing the content of the ^{29}Si isotope. Further narrowing of the EPR line requires a decrease in the concentration of the ^{13}C isotope.

The T_1 times measured in $6H$-^{28}SiC crystal (sample #2) at the X band at 300 and 100 K in $B \parallel c$ and $B \perp c$ orientations under 785 nm optical excitation are presented in Table II.

An orientation dependence of the relaxation time is observed, and the relaxation rate in the case of magnetic field directed along the axis of the defect (crystal c axis) and perpendicular to it differs by a factor of two. The relaxation times T_1 are significantly longer than $6H$-SiC crystal, with the natural content of isotopes, considered in the previous section.

D. Rabi oscillations

A Rabi cycle and the inverse of its duration as a Rabi frequency is the cyclic behavior of a two-level quantum system in the presence of an oscillatory driving field. Any two-state quantum system, e.g., a spin-$\frac{1}{2}$ system with magnetic moment $\boldsymbol{\mu}$ placed in a magnetic field $\mathbf{B}$, can be used to form a qubit. Rabi oscillations or transient nutation are the basic processes used to manipulate qubits and have crucial importance in quantum computing. These oscillations are obtained by exposing qubits to periodic magnetic or electric fields (driving field) during suitably adjusted time intervals.

To detect transient nutation (Rabi oscillations), as a rule, two types of experiments are used: FID and ESE. The objective of the transient nutation experiment is twofold. Firstly, it allows one to establish the fact that coherence can be created. Secondly, from the transient nutation experiment, the duration of $\pi/2$ and π pulse can be established, which is necessary for ESE experiments.

1. FID-detected Rabi oscillations

Figure 5(a, top) shows a pulse sequence for the measurement of Rabi oscillations with FID detection of transient nutation after a nutation pulse of variable duration t_1; the dead time of the spectrometer is denoted by t_d.

FID is most clearly seen after the $\pi/2$ pulse. It is a short-lived sinusoidal electromagnetic signal appearing immediately following the $\pi/2$ pulse. The decay of the FID after the $\pi/2$ pulse is determined by T_2^*, i.e., by the total inhomogeneous linewidth. In Fig. 5(b), the resulting inhomogeneous resonance line with linewidth $\Delta\omega_{inhom} = 2T_2^{*-1}$ is presented. In the inhomogeneous line, the homogeneous line with linewidth $\Delta\omega_{hom} = 2T_2^{-1}$ is indicated. Thus, FID is a destruction of the phase coherence of the spin ensemble due to inhomogeneous broadening. Usually, the FID is very fast and obscures all other dynamical processes which give rise to dephasing.

The FID decays exponentially with a time constant of T_2^* according to $[\sin\omega_0 t] \times \exp(-t/T_2^*)$. We used the simplest approximation, when T_2^* demonstrates a decay in signal intensity by a factor of e. The more complex approximations are usually used when the nature of relaxation processes is being investigated. Note that, in our case, the relaxation processes proceed simultaneously with the optical alignment of the spin level populations; that is, in the kinetic equations describing changes in the populations of spin levels, it is necessary to add optically induced effects. In practice, part of the FID is inaccessible due to dead time t_d. The EPR FID signal often decays within the dead time of the spectrometer. To overcome this limitation, two-pulse ESE is used. The effect of inhomogeneous broadening can be circumvented by applying microwave pulses in special pulse sequences.

2. ESE-detected Rabi oscillations

The dead time problem in the FID-detected Rabi oscillations can be solved by observing an ESE (or Hahn echo). ESE detection of longitudinal magnetization after a nutation pulse of variable duration t_1 is shown in the bottom of Fig. 5(a). A delay time T is inserted after a nutation pulse of variable duration t_1. T is much longer than t_1 and T_2^*, but smaller than T_1, such that the perpendicular magnetization component has vanished and electron coherence decays completely. Then after the waiting time T, a standard two-pulse ESE sequence of duration τ is used to measure the longitudinal magnetization component $M_Z(t)$. The change in polarization induced by the nutation pulse is then detected by ESE. An ESE produced by a π pulse following a $\pi/2$ pulse appears as a back-to-back FID where the signal increases exponentially to the middle of the signal then decreases exponentially like the FID. The refocusing of the magnetization of the individual spin packets only works if the "fast" spins remain fast and the "slow" spins remain slow. If there are random jumps in the resonance frequency of the spin packets in the time interval 2τ, then this effect will be observed as a decay of the ESE with increasing time 2τ. The decay function of ESE intensity as a function of 2τ gives the rate of irreversible loss of phase coherence, i.e., the relaxation time T_2. In other words, whereas the decay of the FID after a $\pi/2$ pulse is determined by T_2^*, i.e., by
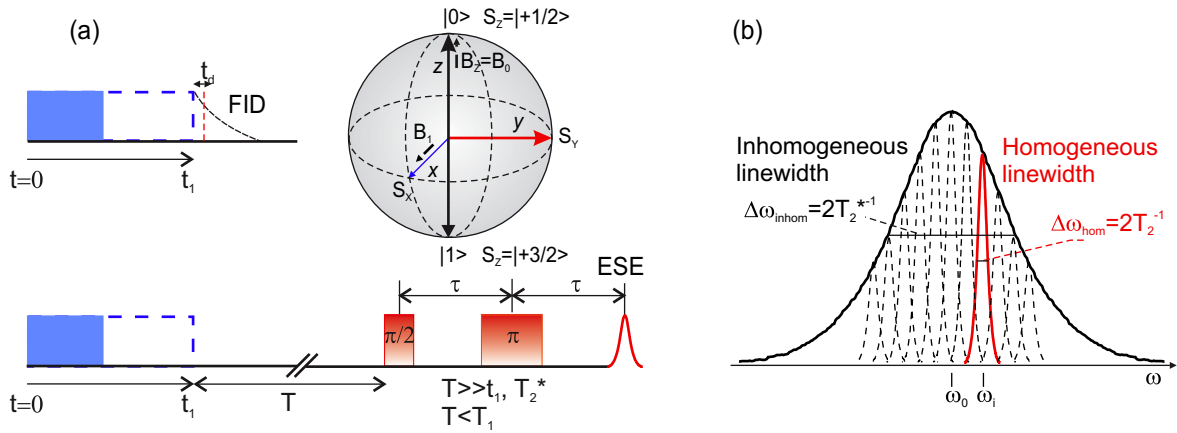
FIG. 5. (a) Pulse sequences for the measurement of Rabi oscillations: (top) free induction decay (FID) detection of transient nutation after a nutation pulse of variable duration t_1; (bottom) electron spin echo (ESE) detection of longitudinal magnetization after a nutation pulse of variable duration t_1. A waiting time T much longer than T_2, but smaller than T_1. After time T, a standard Hahn echo sequence of duration τ is used to measure the magnetization component $M_Z(t)$. The dead time of the spectrometer is denoted by t_d. (Inset) Definition of different spin states on the Bloch sphere, which is a geometrical representation of the pure state space (points on the surface of the sphere) of a two-level quantum mechanical system (qubit). The north and south poles of the Bloch sphere are typically chosen to correspond to the standard basis vectors $|0\rangle$ and $|1\rangle$, respectively, which in turn might correspond, e.g., to the spin-up and spin-down states of an electron. The qubit oscillates between the $|0\rangle$ and $|1\rangle$ states. (b) The resulting inhomogeneous resonance line with linewidth $\Delta\omega_{\mathrm{inhom}} = 2T_2^{*-1}$. In the inhomogeneous line, the homogeneous line, "spin packet", with linewidth $\Delta\omega_{\mathrm{hom}} = 2T_2^{-1}$ is indicated.

the total inhomogeneous linewidth, the decay of the spin echo signal as a function of 2τ is determined by T_2, i.e., by the homogeneous linewidth [see Fig. 5(b)]. The inhomogeneous linewidth is caused by both instrumental effects and local fields: the individual spins not only feel the externally applied magnetic field but also the local fields produced by their neighbors. There is a spread $\Delta\omega_0$ in the values ω_0 of the individual spins in the sample. The result is a resonance line with an inhomogeneous linewidth that is determined by the field gradient over the sample. The homogeneous linewidth $\Delta\omega_{\mathrm{hom}}$ then is only a fraction of the experimentally observed inhomogeneous linewidth [Fig. 5(b)]. One usually describes the homogeneous linewidth ("spin packet") by a relaxation time T_2 to indicate that the homogeneous linewidth is roughly $2T_2^{-1}$.

The inset in Fig. 5(a) shows a definition of different spin states on the Bloch sphere. The Bloch sphere is a geometrical representation of the pure state space (points on the surface of the sphere) of a two-level quantum mechanical system or qubit. The north and south poles of the Bloch sphere are typically chosen to correspond to the standard basis vectors $|0\rangle$ and $|1\rangle$, respectively, which in turn might correspond, e.g., to the spin-up and spin-down states of an electron. The qubit oscillates between the $|0\rangle$ and $|1\rangle$ states. The maximum amplitude for oscillation is achieved at $\omega = \omega_0 = |\gamma|B_0$, which is the condition for resonance. At resonance, the transition probability is given by $P_{0\rightarrow 1}(t) = \sin^2(\omega_R t/2)$, where Rabi frequency $\omega_R = |\gamma||B_1|$. The equilibrium magnetization **M** in external magnetic field, which at time $t = 0$ is parallel to the constant magnetic field $B_z = B_0$, starts a precession under the influence of the resonant microwave field with amplitude B_1 in a frame rotation in the zy plane at the resonance frequency. It is assumed, e.g., that the microwave field is polarized along the x axis. The result is that the magnetization M_z oscillates in time according to $M_Z(t) = M_0\cos\omega_R t$ with Rabi frequency

ω_R, which depends on microwave power. To go from state $|0\rangle$ to state $|1\rangle$, it is sufficient to adjust the time t during which the rotating field acts such that $t = \pi/\omega_1$. This is called a π pulse. For $t = \pi/2\omega_1$, we have a $\pi/2$ pulse, which acts as $|0\rangle \rightarrow (|0\rangle + i|1\rangle)/\sqrt{2}$. This operation has crucial importance in quantum computing.

Observed Rabi nutations persist for tens of microseconds at RT and evidence that the probed spin ensemble can be prepared in a coherent superposition of the spin states in resonant magnetic fields at RT. In addition, the electron spin of the spin-$\frac{3}{2}$ centers can be manipulated by low-frequency microwave field 30–130 MHz, which is compatible with nuclear magnetic resonance imaging. The accent is made on the spin color centers, which are optically active in the near-infrared spectral region, which is preferential for potential *in vivo* biological applications due to the deepest tissue penetration and which is compatible with fiber optics.

To clearly demonstrate the relaxation processes, experiments were performed to measure the Rabi oscillations and establish the dependence of the Rabi frequency on the amplitude of the oscillation magnetic field B_1. We study the decay time of the Rabi oscillations for spin centers at two temperatures 300 and 100 K. Figure 6 shows long-lived Rabi oscillations measured in the X band as an ESE intensity vs nutation pulse length (Δt) at a temperature of (a) 300 K and (b) 100 K in a $6H$-^{28}SiC crystal (sample #2). Thus, we have RT coherent spin manipulation of the spin-$\frac{3}{2}$ center ensemble in $6H$-SiC. Figure 6(c) shows measured Rabi frequencies ($\omega_R = 2\pi f_R$) extracted from Rabi oscillation [Figs. 6(a) and 6(b)] and converted microwave field (B_1) strength vs the square root of the total microwave power applied to the sample. For conversion, $f_R = \sqrt{3}g\mu_B B_1/h$ is used.

The observed oscillatory behavior demonstrates that the probed spin center ensemble in SiC can be prepared in a coherent superposition of the spin states at resonant
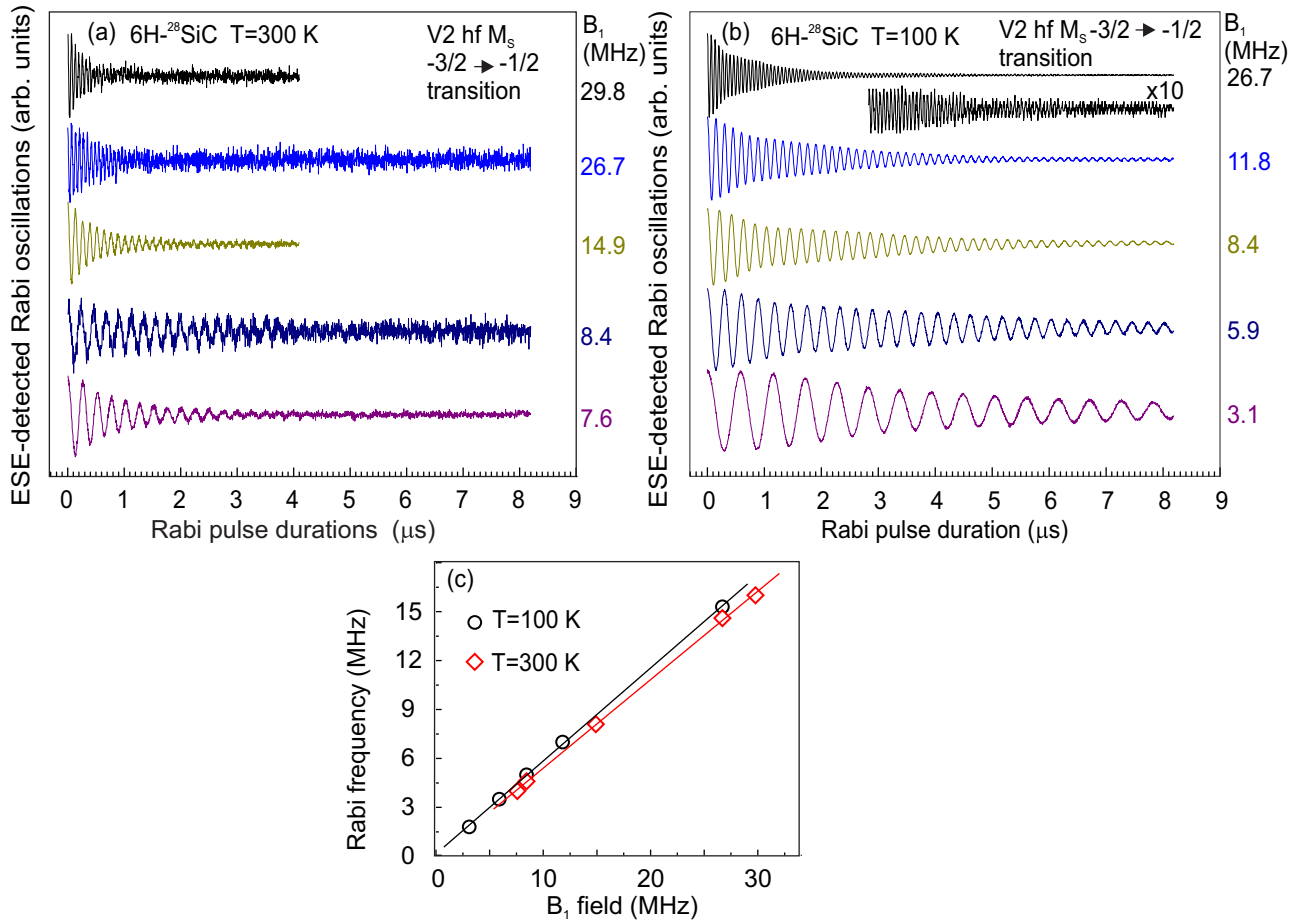
FIG. 6. Electron spin echo (ESE)-detected Rabi oscillations in the X band at a temperatures of (a) 300 K and (b) 100 K in a $6H$-^{28}SiC crystal (sample #2). (c) Measured Rabi frequencies ($\omega_R = 2\pi f_R$) in $6H$-^{28}SiC crystal on high-field (hf) transition of the V2 center, extracted from Rabi oscillation [Figs. 6(a) and 6(b)] and converted microwave field (B_1) strength vs the square root of the total microwave power applied to the wire. For conversion, $f_R = \sqrt{3}g\mu_B B_1/h$ is used. The dependence is linear both at 100 K and at room temperature (solid lines are linear fit); the slope of two approximating straight lines coincides within the error limits.

magnetic fields at RT. A population difference of the spin states becomes modulated in time with the Rabi frequency. Rabi oscillations decay with a characteristic time constant that depends on the microwave power. The oscillation of M_Z damps because of the spread in B_1 values over the sample because of the inhomogeneity of the microwave field. This leads to a fanning out of the ensemble of spins in the zy plane (rotating frame B_1 is directed along the x axis). When this fanning out covers the whole disc, the resulting value of $M_Z = 0$. One will conclude that the transition is saturated because, macroscopically seen, the two spin states have the same population.

E. Pulsed ELDOR in *n*-irradiated 6*H*-SiC

Here, we discuss results of the PELDOR experiments on spin-$\frac{3}{2}$ color centers in *n*-irradiated 6*H*-SiC (sample #1). For the system with $S = \frac{3}{2}$ in accordance with the selection rule $\Delta M_S = \pm 1$, three resonance transitions should occur ($-\frac{3}{2} \rightarrow -\frac{1}{2}$), ($-\frac{1}{2} \rightarrow +\frac{1}{2}$), and ($+\frac{1}{2} \rightarrow +\frac{3}{2}$).

Figure 7(a) shows ESE-detected Rabi oscillations at a temperature of 300 K on high-field transition of V1/V3 centers in neutron irradiated 6*H*-SiC crystal (sample #1).

(b) Measured Rabi frequencies extracted from Rabi oscillation [Fig. 7(a)] and converted microwave field B_1 are depicted in Fig. 7(b). The dependence is linear (solid lines are linear fits). In Fig. 7(c), evidence is presented that the decay of Rabi oscillations of spin qubit ensembles depends noticeably on the microwave power and more precisely on the Rabi frequency, an effect known as "driven decoherence" [26].

To begin with, we measure the reference ESE-detected EPR spectra of V2 and V1/V3 centers in 6*H*-SiC. Figure 8(a) shows the ESE spectrum recorded at RT under 785 nm optical excitation; magnetic field is parallel to the c axis. The inset shows a pulse sequence for detecting ESE. Two pairs of the outer resonances correspond to ($+\frac{1}{2} \rightarrow +\frac{3}{2}$; emission of the resonant microwaves) and ($-\frac{3}{2} \rightarrow -\frac{1}{2}$; absorption) transitions between the spin sublevels of V2 and V1/V3 centers. In accordance with the results of several experiments, $M_S = \pm\frac{1}{2}$ are equally populated under optical excitation. Thus, ($-\frac{1}{2} \rightarrow +\frac{1}{2}$) cannot be detected due to the absence of the resonant microwave absorption-emission between these two states. In addition, we cannot ascribe the central line to the ($-\frac{1}{2} \rightarrow +\frac{1}{2}$) because it is hidden and mixed
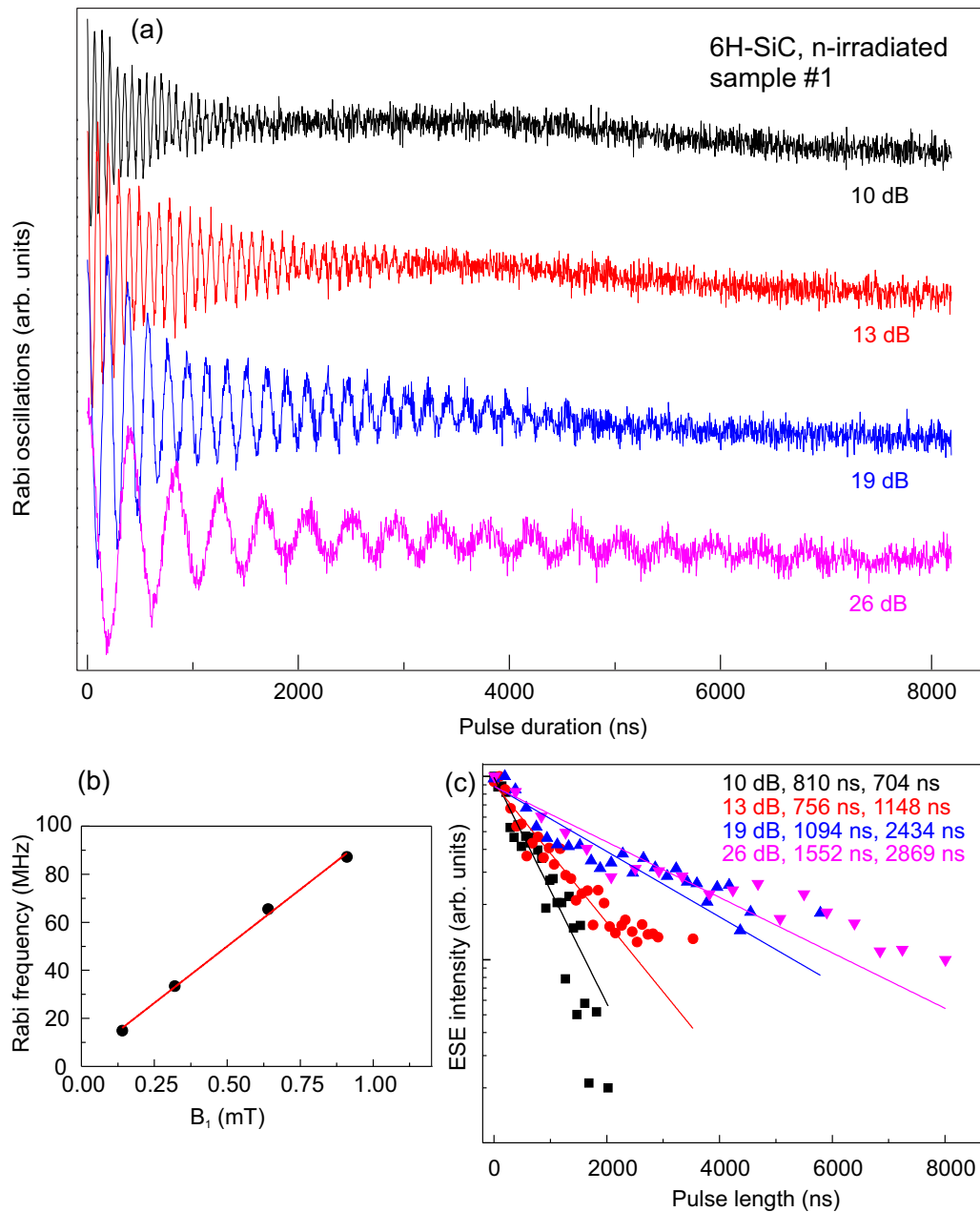
FIG. 7. (a) Electron spin echo (ESE)-detected Rabi oscillations at a temperature of 300 K on high-field transition of V1/V3 center in neutron-irradiated 6H-SiC crystal (sample #1). (b) Measured Rabi frequencies extracted from Rabi oscillation [Fig. 7(a)] and converted microwave field B_1. The dependence is linear (solid lines is linear fit). (c) Evidence that the decay time of Rabi oscillations of ensembles of spin qubits depends noticeably on the microwave power and more precisely on the Rabi frequency, an effect recently called "driven decoherence" [26].

with the signal of the negatively charged silicon vacancy (V_{Si}^-) in regular defect-free environment.

The essence of the PELDOR method is that a change in the intensity of the ESE signal corresponding to one of the spin-allowed transitions is recorded depending on the sweep of the second frequency. With a resonant coincidence of the sweep frequency with another allowed transition associated with the former, a change in the intensity of the latter is observed. PELDOR, a double-resonance technique, gives us an opportunity to detect existence of the ($-\frac{1}{2} \rightarrow +\frac{1}{2}$) transition. This can be done if the population differences between $+\frac{1}{2}$

or $-\frac{1}{2}$ sublevels are enough to detect what can be achieved by applying the second microwave pulse (mw2) which is resonant to the ($-\frac{3}{2} \rightarrow -\frac{1}{2}$) and ($+\frac{1}{2} \rightarrow +\frac{3}{2}$) transitions. We performed experiments to measure the FID signal when scanning the additional microwave frequency. Such an approach is like the ENDOR technique, but in PELDOR, the detection is done by monitoring the fine structure transitions instead of HF transitions in ENDOR.

Figure 8(b) shows the PELDOR spectrum of the V1/V3 centers. Here, we are measuring the changes in the FID signal intensity at the resonant conditions for the ($-\frac{1}{2} \rightarrow +\frac{1}{2}$) tran-
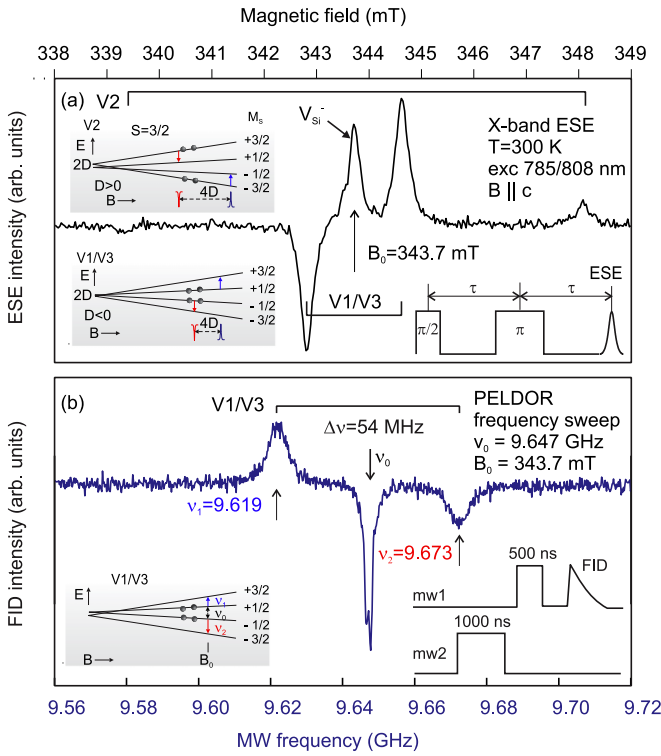
FIG. 8. (a) Electron spin echo (ESE) spectrum of V2 and V1/V3 centers in 6H-SiC (sample #1) recorded at room temperature (RT) when the magnetic field was oriented parallel to the hexagonal axis (c axis) of the crystal under optical excitation at $\lambda = 785$ nm; (inset) pulse sequence for detecting ESE. (b) RT coherent control of V1/V3 spin-$\frac{3}{2}$ centers in 6H-SiC: pulsed electron-electron double resonance (PELDOR) spectrum detected at RT at magnetic field $B = 343.7$ mT and microwave frequency mw1 = 9.647 GHz by sweeping the frequency mw2 of the second microwave pulse; (inset) pulse sequence for detecting PELDOR by the measuring of the free induction decay (FID). Arrows indicate positions of two resonance transitions: $(-\frac{3}{2} \rightarrow -\frac{1}{2})$ and $(+\frac{1}{2} \rightarrow +\frac{3}{2})$; central line is due to coincidence between mw1 and mw2 pulses. The inset shows the V1/V3 spin-$\frac{3}{2}$ splitting with growing magnetic field. The circles represent the pumped $M_S = \pm\frac{1}{2}$ (depleted $M_S = \pm\frac{3}{2}$) states. The vertical arrows indicate the microwave frequency-induced spin transitions.
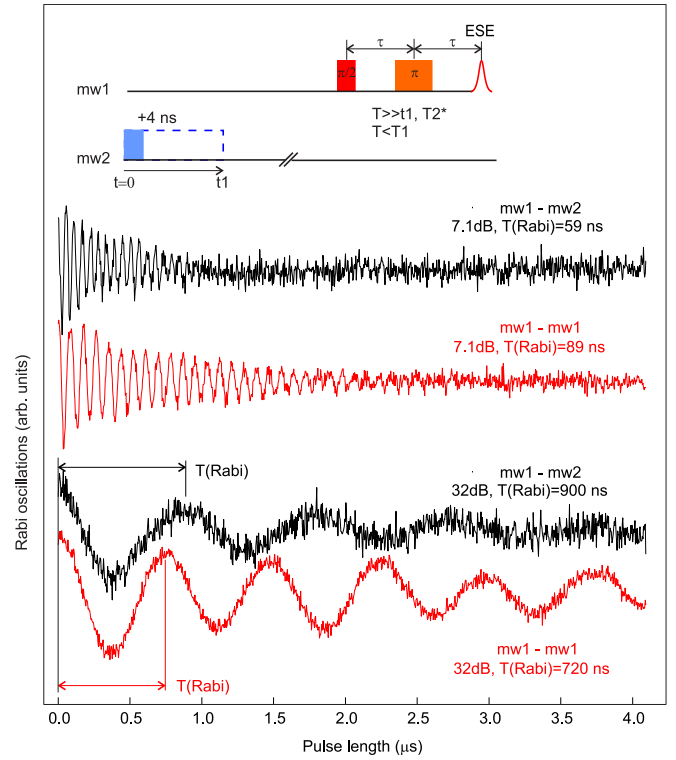

FIG. 9. Electron spin echo (ESE)-detected Rabi oscillations at a temperature of 300 K on high-field transition of V1/V3 centers in neutron-irradiated 6H-SiC crystal (sample #1) using a modified pulse sequence, shown in the top. The decay time of the Rabi oscillations becomes shorter when the first microwave pulse mw1 excites a lateral transition $|\frac{1}{2}\rangle \rightarrow |\frac{3}{2}\rangle$ rather than a center transition $|-\frac{1}{2}\rangle \rightarrow |\frac{1}{2}\rangle$. Thus, the measurements presented in Figs. 7–9 demonstrate the possibilities for spin manipulations using several frequencies, which cause resonance transitions between different spin levels.

sition between spin sublevels of the V3 center: magnetic field is set at $B_0 = 343.7$ mT, and resonant microwave frequency (mw1) at $\nu_0 = 9.647$ GHz is applied. We sweep the frequency of mw2 in the range of several hundred MHz. The pulse sequence of frequencies for detection of the PELDOR spectra is shown in the inset in Fig. 8(b). Two well-pronounced resonance transitions at frequencies $\nu_0 = 9.619$ and 9.673 GHz appear. The energy separation between these transitions is 54 MHz, equal to the doubled ZFS of the center (2×27 MHz for V1/V3). This is expected when magnetic field is parallel to the quantization z axes of the fine structure tensor ($B||c$ and $c||z$).

At $\nu_0 = 9.619$ GHz, we detect a low energy $(-\frac{3}{2} \rightarrow -\frac{1}{2})$ transition. At $\nu_0 = 9.673$ GHz, higher energy $(+\frac{1}{2} \rightarrow +\frac{3}{2})$ transition is observed. The signal at $\nu_0 = 9.647$ GHz is due to the resonant coincidence of mw1 and mw2 pulses. All lines are detected by monitoring the resonance conditions of

"hidden" $(-\frac{1}{2} \rightarrow +\frac{1}{2})$ transition and can be observed only if such a transition exists. Moreover, this experiment shows the possibility to coherently detect the optical spin alignment between $M_S = \pm\frac{3}{2}$ via optically pumped silent $M_S = \pm\frac{1}{2}$ sublevels of the V1/V3 centers. Similar PELDOR spectra were recorded at the V2 center in 6H-SiC.

To manipulate the spin states of the spin-$\frac{3}{2}$ center, we used a modified pulse sequence for recording the Rabi oscillations indicated in Fig. 9. Figure 9 shows ESE-detected Rabi oscillations at a temperature of 300 K on high-field transition of V1/V3 centers in neutron-irradiated 6H-SiC crystal (sample #1). A modified pulse sequence, shown at the top, was used. The decay time of the Rabi oscillations becomes shorter when the first microwave pulse mw1 excites a lateral transition $|\frac{1}{2}\rangle \rightarrow |\frac{3}{2}\rangle$ rather than the center transition $|-\frac{1}{2}\rangle \rightarrow |\frac{1}{2}\rangle$. Thus, the measurements presented in the Figs. 7–9 demonstrate the possibilities for spin manipulations using several frequencies, which cause resonance transitions between different spin levels.

IV. DISCUSSION

As shown above, a sharp decrease of the spin-lattice relaxation time T_1, ~40 times, was observed in high magnetic

field with increasing temperature from 100 to 300 K, while the spin-spin relaxation time T_2 is only shortened by ~1.3 times; that is, it is almost independent on temperature.

Comparison of the values of T_1 and T_2 at different temperatures shows that the mechanism that determines spin-lattice relaxation time T_1 differs significantly from the mechanism of spin-spin relaxation time T_2. We did not conduct a detailed study of the temperature dependences of relaxation processes, including low temperatures, since the main goal of this paper was to demonstrate high coherent properties of spin centers at temperatures close to RT. Nevertheless, the performed fitting of the temperature dependences for the rate $1/T_1$ leads to the conclusion that a Raman process plays the main role. It should be noted that all relaxation processes take place under conditions of optical alignment of the spin level populations. Moreover, the relaxation characteristics are measured at EPR transitions with both the absorption of resonance microwave energy and its emission.

The rate $1/T_2$ is slightly temperature dependent. A general case following the Ref. [27] behavior of the spin-spin relaxation time T_2 in a form of the resulting spin decoherence rate can be described by the following equation:

$$\frac{1}{T_2} \propto \frac{1}{T_2(n)} + \frac{1}{T_2(d)} + \frac{1}{T_2(\mathrm{slr})}. \quad (2)$$

It is believed that the first term $1/T_2(n)$ is a result of nuclear spins ^{13}C and ^{29}Si flip-flopping; the second term $1/T_2(d)$ is due to an interaction with paramagnetic defects: irradiation-induced defects, paramagnetic impurities, among which shallow nitrogen donors (substitutional nitrogen in the neutral charge state $S = \frac{1}{2}$) play an important role. The third term $1/T_1(\mathrm{slr})$ is due to the influence of spin-lattice relaxation T_1 on T_2.

The impact of the first two terms is temperature independent, until very extreme conditions with high Boltzmann factors such as low temperatures and high magnetic fields at which sufficient electron-nuclear spin polarization occurs (see Ref. [28]). Thus, only one term $1/T_1(\mathrm{slr})$ in Eq. (2) is temperature dependent. As follows from the above equation, since for the spin-$\frac{3}{2}$ centers in SiC sample under study $T_1 = 42.4\,\mu$s is much longer than $T_2 = 5.6\,\mu$s even at RT, we do not expect strong T_1 temperature dependence to induce sufficient increment of the T_2.

As noted above, the electron spin coherence time T_2 is inversely proportional to the concentration of nuclear spins [17], so two types of nuclear spins ^{13}C and ^{29}Si contribute to the decoherence of spin centers in SiC [$1/T_2(n)$ term in Eq. (2)]. Following Refs. [17] and [23], it is reasonable to use nitrogen-vacancy centers in diamond as a simplest reference point with which we will compare the spin bath concentration. The effective nuclear spin bath concentration of SiC, considering two independent nuclear spin baths, is estimated as $\rho_{\mathrm{SiC}} = 0.5 \times \eta_{\mathrm{V}}(\rho_{\mathrm{C13}} + \rho_{\mathrm{Si29}} \times \eta_\gamma)$, where $\eta_\gamma = (\gamma_{\mathrm{Si29}}/\gamma_{\mathrm{C13}})^2 = 0.63$; the unit cell volume expansion of SiC comparing with diamond can be expressed as the ratio $\eta_{\mathrm{V}} = (d_{\mathrm{C\text{-}C}}/d_{\mathrm{Si\text{-}C}})^3 = 0.55$, where $d_{\mathrm{Si\text{-}C}} = 1.88$ Å and $d_{\mathrm{C\text{-}C}} = 1.54$ Å are the Si-C and C-C bond lengths in SiC and diamond, respectively. Smaller gyromagnetic ratio of ^{29}Si ($\gamma_{\mathrm{Si29}} = -2\pi \times 0.85$ kHz/G) compared with that of ^{13}C ($\gamma_{\mathrm{C13}} = 2\pi \times 1.07$ kHz/G) reduces the nuclear spin bath flipping rate of the

^{29}Si bath. Thus, the effective nuclear spin concentration of SiC is like that of diamond, i.e., $\rho_{\mathrm{SiC}}/\rho_{\mathrm{diamond}} \approx 1$. Consequently, the nuclear spin bath in SiC with natural isotope content should cause similar electron spin decoherence rate as ^{13}C in diamond with natural isotope content. Thus, even though the natural abundance of ^{29}Si is ~4 times larger than that of ^{13}C, the T_2 time of spin color centers in SiC is not reduced significantly. A decrease in the ^{29}Si content by a factor of ~5, $\rho_{\mathrm{SiC}}/\rho_{\mathrm{diamond}}$ is reduced by a factor of ~2: with $\rho_{\mathrm{Si29}} = 0.9\%$ in our experiments, the ratio $\rho_{\mathrm{SiC}}/\rho_{\mathrm{diamond}}$ is of 0.46.

According to Ref. [29], the spin-lattice relaxation time T_1 remains constant up to high irradiation densities, regardless of the type of irradiation. This is expected, since the dominant effect that determines the time T_1 is spin-phonon scattering, which as an intrinsic property of the crystal does not depend on the fluence up to a certain level. These findings give grounds to the claim that the temperature dependences of the times T_1 can be compared in crystals under study (samples #1, #2, and #3) irradiated with both neutrons (sample #1) and electrons (samples #2 and #3). T_1 and T_2 of spin-$\frac{3}{2}$ centers in neutron-irradiated 6H-SiC crystal (sample #1) are equal to 1.7 ms and 7.17 μs, respectively. Comparison with the corresponding times in electron-irradiated commercial 6H-SiC crystal (sample #3), $T_1 = 3.4$ ms and $T_2 = 44\,\mu$s (see Supplemental Material [24]), gives grounds to assert that neutron irradiation leads to shorter relaxation times of spin-$\frac{3}{2}$ centers than electron irradiation. Note that the concentration of spin-$\frac{3}{2}$ centers in both samples is approximately the same.

In contrast to T_1, the spin-spin relaxation time T_2 is sensitive to the type and fluence of irradiation particles, which indicates a much higher T_2 sensitivity with respect to interactions between defects than the time T_1. Thus, T_2 is longer under electron irradiation; the shortest T_2 is observed in neutron-irradiated samples due to irradiation-induced defects.

One of the main problems of using spin centers in systems of quantum calculations and sensorics is the control of the concentration of paramagnetic nitrogen donors, spin interactions which cause the loss of the coherent properties of spin centers [$1/T_2(d)$ term in Eq. (2)]. Furthermore, this problem is even more serious in SiC than NV centers in diamond since nitrogen donors in diamond are characterized by deep levels in the band gap, i.e., are rather highly localized. In contrast, nitrogen donors in SiC are characterized by shallow levels; as a result, their wave functions are strongly delocalized. The "effective Bohr radius" a^* for the electron wave function in 4H-SiC is $a^* \approx 13$ Å and in 6H-SiC is $a^* \approx 7.2$ Å [30,31]. For many applications, the effect of the spin system of donor nitrogen on coherent properties of spin-$\frac{3}{2}$ centers should be minimized. It was found [30,31] that the spin density of the nitrogen donor electron propagates mostly over silicon atoms in 4H-SiC. In contrast, the spin density of the nitrogen donor electron propagates mostly over carbon atoms in 6H-SiC. Since carbon atoms are nearest to the silicon vacancy, it can be assumed that exactly these atoms will mainly contribute to spin relaxation of unpaired electrons of the silicon vacancy-related spin-$\frac{3}{2}$ center. Thus, paramagnetic centers in the 4H-SiC polytype can be more stable to interactions with unpaired donor electrons since electrons are not localized on the coordination sphere nearest to the paramagnetic center in

this case. From this point of view, 4*H*-SiC has advantages over 6*H*-SiC, but it should also be considered that the Bohr radius of an electron in 6*H*-SiC is almost two times smaller than that in 4*H*-SiC, which gives some advantage to 6*H*-SiC. Thus, it is important to emphasize that it is necessary to reduce the concentration of nitrogen donors. Unlike diamond, nitrogen is not a building base for spin color centers, which have an intrinsic structure in SiC. Thus, the nitrogen concentration can theoretically be reduced to the technologically possible limit.

The spin-echo experiments are not specific for the precession of spins in a magnetic field. They apply to any two-level system in interaction with a coherent radiation field. Using the logic of magnetic resonance, it is not *a priori* clear whether it is possible to describe transient phenomena in zero magnetic field, using the model of precession of the magnetic moment in a magnetic field [32]. In zero magnetic field, there is no Zeeman interaction, and the anisotropy of the interactions of the spin system with the microwave field is determined by the symmetry of the crystal field causing the ZFS. The resonance in spin-$\frac{3}{2}$ is due to a nonzero matrix element of the transition between, e.g., $|+\frac{1}{2}\rangle$ and $|+\frac{3}{2}\rangle$ levels caused by interaction with a resonant microwave field. Since the two GSs $|+\frac{1}{2}\rangle$ and $|+\frac{3}{2}\rangle$ are assumed to have an identical electron distribution, the transition cannot be induced by the electric component of the radiation field; however, it is allowed as a magnetic dipole transition.

A simple, rigorous geometrical representation for the time-dependent Schrödinger equation was developed [33] to describe the behavior of an ensemble of two quantum-level, noninteracting systems which are under the influence of a perturbation. This transformation (so-called "Feynman-Vernon-Hellwarth transformation") has several advantages: First, it is possible to make a pictorial representation of an evolution of any two-level quantum system. Second, inspiration can be drawn from the various transient phenomena known in magnetic resonance to describe similar experiments with coherent microwave or light sources. It can be shown [32,33] that the evolution of the two-level system, formed, for instance, by the $|+\frac{1}{2}\rangle$ and $|+\frac{3}{2}\rangle$ sublevels in interaction with a resonant microwave field $V(t) = g\mu_B \mathbf{B}_1 S\cos\omega t$ $(g\mu_B = \gamma\hbar)$, can be described by an equation of motion in the form of the real three-dimensional vector equation that is identical in form to the equation of motion of a magnetic moment in a magnetic field $d\mathbf{M}/dt = -\gamma\mathbf{B}\times\mathbf{M}$ and, when suitable relaxation terms are added, is identical to the Bloch equations. This equation is $d\mathbf{r}/dt = \mathbf{\Omega}\times\mathbf{r}$, where the components of the vector $\mathbf{r}$ uniquely determine the wave function $\Psi(t) = a(t)\Psi_a + b(t)\Psi_b$ of a given two-level system and the components of $\mathbf{\Omega}$ represent the perturbation. Here, Ψ_a and Ψ_b are the two eigenstates of interest of the Hamiltonian for the single system $\psi_a = |+\frac{1}{2}\rangle$ and $\psi_b = |+\frac{3}{2}\rangle$ for the GS of spin-$\frac{3}{2}$ center. In this case, the presence of the other levels may be neglected, simplifying the spin-$\frac{3}{2}$ system to a two-level system. The vector $\mathbf{r}$ can be considered as a "pseudomagnetization" precessing about a "pseudofield" $\mathbf{\Omega}$. Then $r_1 = ab^* + ba^*$, $r_2 = i(ab^* - ba^*)$, and $r_3 = aa^* - bb^*$; and $\Omega_1 = (V_{ab} + V_{ba})/\hbar$, $\Omega_2 = (V_{ab} - V_{ba})/\hbar$, and $\Omega_3 = \omega_0$; and $V_{ab} = -V_{ba} = \langle +\frac{1}{2} + |V(t)| + \frac{3}{2}\rangle$. Equivalently, here the

pseudomagnetization vector $\mathbf{r}$ precesses around the quasifield $\mathbf{\Omega}$. The component r_3 represents a normalized population difference of the $|+\frac{1}{2}\rangle$ and $|+\frac{3}{2}\rangle$ sublevels; the magnitude of r_1 and r_2 is a measure of the amount of coherence.

In the case of high-field magnetic resonance of spin-$\frac{1}{2}$ particles, $\mathbf{r}$ space reduces to physical space; Ω_3 turns out to be proportional to the static field, while Ω_1 and Ω_2 are proportional to the oscillation microwave magnetic field components perpendicular to the static field. In the zero magnetic field two-level system (e.g., $+|\frac{1}{2}\rangle$, $+|\frac{3}{2}\rangle$ levels) of spin center Ω_3 is simply frequency ω_0, which corresponds to the ZFS $\Delta = \hbar\omega_0$, while Ω_1 and Ω_2 is proportional to the microwave perturbation. It is important to emphasize that both in experiments in zero magnetic field and in fixed magnetic fields, the Rabi frequency is of $\omega_R = |\gamma|B_1$.

V. SUMMARY

The coherent spin manipulations of spin-$\frac{3}{2}$ ensembles in 6*H*-SiC crystal in high magnetic fields have been demonstrated over a wide temperature range, including RT. A sharp decrease of spin-lattice relaxation time T_1, $\sim$40 times, from 1.7 ms to 42 μs, was observed in magnetic field of $\sim$3.5 T with increasing temperature from 100 to 300 K, while the spin-spin relaxation time T_2 is only shortened by $\sim$1.3 times, from 7.2 to 5.6 μs; that is, it is almost independent of temperature.

Comparison of T_1 and T_2 for spin-$\frac{3}{2}$ centers in neutron-irradiated 6*H*-SiC crystal, 1.7 ms and 7.17 μs, respectively, with the corresponding times in electron-irradiated crystal (commercial 6*H*-SiC wafer, see Supplemental Material [24]), $T_1 = 3.4$ ms, $T_2 = 44$ μs, gives grounds to assert that neutron irradiation leads to shorter relaxation times than electron irradiation. The neutron irradiation leads to the creation of many paramagnetic defects, which results in a sixfold decrease in time T_2 and twofold decrease in time T_1. However, the relaxation times were concluded to be long enough for applications. An increase in the magnetic field leads to a reduction of the times T_1 and T_2. An orientation dependence of the relaxation time T_1 was observed: T_1 in the case of magnetic field directed along the axis of the spin-$\frac{3}{2}$ center (crystal *c* axis) is about two times longer than T_1 in magnetic field perpendicular to the crystal *c* axis. When going from spin-$\frac{3}{2}$ center V2 to V1/V3, there is an opposite change in the times T_1 and T_2 : T_1 lengthens, and T_2 shortens.

A decrease in the concentration of a silicon isotope ^{29}Si with a nuclear magnetic moment leads to a significant lengthening of the relaxation times. This is because a reduction in the ^{29}Si content by a factor of $\sim$5 (in our experiment), the effective nuclear spin bath ρ_{SiC} in SiC is reduced by a factor of $\sim$2.

The transient nutation (Rabi oscillation) experiments allowed us to establish the fact that spin coherence can be created at RT. Evidence was presented that the decay time of Rabi oscillations of ensembles of spin qubits depends distinctly on the microwave power and more precisely on the Rabi frequency, so-called driven decoherence [26,34].

It was experimentally demonstrated that an ESE can be observed both for a spin-$\frac{3}{2}$ ensemble in zero magnetic field and in strong magnetic field. Moreover, the Rabi frequency in both cases is equal for the same amplitude of B_1. In zero magnetic field, there is no Zeeman interaction, and the anisotropy of the interactions of the spin system with the microwave field is determined by the symmetry of the crystal field causing the ZFS. Resonance transitions are allowed as magnetic dipole transitions with frequency ω_0 which correspond to the ZFS of spin-$\frac{3}{2}$ center $\Delta = \hbar\omega_0$. So-called Feynman-Vernon-Hellwarth transformation [33] can be used to describe a behavior in time of both systems. It was introduced in equation $d\mathbf{r}/dt = \mathbf{\Omega} \times \mathbf{r}$, which is isomorphic with the torque equation $d\mathbf{M}/dt = -\gamma \mathbf{B} \times \mathbf{M}$ from magnetic resonance, which describes the time dependence of a magnetic moment in the presence of a magnetic field. Equivalently, here, the pseudomagnetization vector $\mathbf{r}$ precesses around the quasifield $\mathbf{\Omega}$. The component r_3 represents a normalized population difference; the magnitude of r_1 and r_2 is a measure of the amount of coherence.

Experiments have demonstrated that spin manipulation in a spin-$\frac{3}{2}$ ensemble can be effectively performed using several close frequencies, that is, using the PELDOR method under optical excitation. A change in the intensity of the FID signal corresponding to one of the spin-allowed fine structure transitions was recorded depending on the sweep of the second frequency. The possibility to coherently detect the optical spin alignment between $M_S = \pm\frac{3}{2}$ via optically pumped silent $M_S = \pm\frac{1}{2}$ sublevels of V1/V3 or V2 centers, including the observation of Rabi oscillations, is demonstrated.

ACKNOWLEDGMENTS

[1] P. G. Baranov, I. V. Il'in, E. N. Mokhov, M. V. Muzafarova, S. B. Orlinskii, and J. Schmidt, EPR identification of the triplet ground state and photoinduced population inversion for a Si-C divacancy in silicon carbide, JETP Lett. **82**, 441 (2005).

[2] P. G. Baranov, A. P. Bundakova, I. V. Borovykh, S. B. Orlinskii, R. Zondervan, and J. Schmidt, Spin polarization induced by optical and microwave resonance radiation in a Si vacancy in SiC: a promising subject for the spectroscopy of single defects, JETP Lett. **86**, 202 (2007).

[3] J. R. Weber, W. F. Koehl, J. B. Varley, A. Janotti, B. B. Buckley, C. G. Van de Walle, and D. D. Awschalom, Quantum computing with defects, Proc. Natl. Acad. Sci. USA **107**, 8513 (2010).

[4] P. G. Baranov, A. P. Bundakova, A. A. Soltamova, S. B. Orlinskii, I. V. Borovykh, R. Zondervan, R. Verberk, and J. Schmidt, Silicon vacancy in SiC as a promising quantum system for single defect and single-photon spectroscopy, Phys. Rev. B **83**, 125203 (2011).

[5] W. F. Koehl, B. B. Buckley, F. J. Heremans, G. Calusine, and D. D. Awschalom, Room temperature coherent control of defect spin qubits in silicon carbide, Nature (London) **479**, 84 (2011).

[6] D. Riedel, F. Fuchs, H. Kraus, S. Väth, A. Sperlich, V. Dyakonov, A. A. Soltamova, P. G. Baranov, V. A. Ilyin, and G. V. Astakhov, Resonant Addressing and Manipulation of Silicon Vacancy Qubits in Silicon Carbide, Phys. Rev. Lett. **109**, 226402 (2012).

[7] V. A. Soltamov, A. A. Soltamova, P. G. Baranov, and I. I. Proskuryakov, Room Temperature Coherent Spin Alignment of Silicon Vacancies in 4*H*- and 6*H*-SiC, Phys. Rev. Lett. **108**, 226402 (2012).

[8] H. Kraus, V. A. Soltamov, D. Riedel, S. Väth, F. Fuchs, A. Sperlich, P. G. Baranov, V. Dyakonov, and G. V. Astakhov, Room-temperature quantum microwave emitters based on spin defects in silicon carbide, Nat. Phys. **10**, 157 (2014).

[9] H. Kraus, V. A. Soltamov, F. Fuchs, D. Simin, A. Sperlich, P. G. Baranov, G. V. Astakhov, and V. Dyakonov, Magnetic field and temperature sensing with atomic scale spin defects in silicon carbide, Sci. Rep. **4**, 5303 (2014).

[10] S. G. Carter, Ö. O. Soykal, P. Dev, S. E. Economou, and E. R. Glaser, Spin coherence and echo modulation of the silicon vacancy in 4*H*-SiC at room temperature, Phys. Rev. B **92**, 161202(R) (2015).

[11] A. L. Falk, P. V. Klimov, V. Ivády, K. Szász, D. J. Christle, W. F. Koehl, A. Gali, and D. D. Awschalom, Optical Polarization of Nuclear Spins in Silicon Carbide, Phys. Rev. Lett. **114**, 247603 (2015).

[12] P. V. Klimov, A. L. Falk, D. J. Christle, V. V. Dobrovitski, and D. D. Awschalom, Quantum entanglement at ambient conditions in a macroscopic solid-state spin ensemble, Sci. Adv. **1**, e1501015 (2015).

[13] H. J. von Bardeleben, J. L. Cantin, E. Rauls, and U. Gerstmann, Identification and magneto-optical properties of the NV center in 4H-SiC, Phys. Rev. B **92**, 064104 (2015).

[14] S. A. Tarasenko, A. V. Poshakinskiy, D. Simin, V. A. Soltamov, E. N. Mokhov, P. G. Baranov, V. Dyakonov, and G. V. Astakhov, Spin and optical properties of silicon vacancies in silicon carbide—a review, Phys. Status Solidi B **255**, 1700258 (2018).

[15] S. Castelletto, B. C. Johnson, V. Ivády, N. Stavrias, T. Umeda, A. Gali, and T. Ohshima, A silicon carbide room-temperature single-photon source, Nat. Mater. **13**, 151 (2013).

[16] D. J. Christle, A. L. Falk, P. Andrich, P. V. Klimov, J. U. Hassan, N. T. Son, E. Janzén, T. Ohshima, and D. D. Awschalom, Isolated electron spins in silicon carbide with millisecond coherence times, Nat. Mater. **14**, 160 (2015).

[17] M. Widmann, S.-Y. Lee, T. Rendler, N. T. Son, H. Fedder, S. Paik, L.-P. Yang, N. Zhao, S. Yang, I. Booker, A. Denisenko, M. Jamali, S. A. Momenzadeh, I. Gerhardt, T. Ohshima, A. Gali, E. Janzien, and J. Wrachtrup, Coherent control of single spins in silicon carbide at room temperature, Nat. Mater. **14**, 164 (2015).

[18] F. Fuchs, B. Stender, M. Trupke, D. Simin, J. Pflaum, V. Dyakonov, and G. V. Astakhov, Engineering near-infrared single-photon emitters with optically active spins in ultrapure silicon carbide, Nat. Commun. **6**, 7578 (2015).

[19] P. G. Baranov, H.-J. von Bardeleben, F. Jelezko, and J. Wrachtrup, *Magnetic Resonance of Semiconductors and Their Nanostructures: Basic and Advanced Applications*, Springer Series in Materials Science, Vol. 253 (Springer-Verlag GmbH, Austria, 2017), Chap. 6.

[20] V. A. Soltamov, C. Kasper, A. V. Poshakinskiy, A. N. Anisimov, E. N. Mokhov, A. Sperlich, S. A. Tarasenko, P. G. Baranov, G. V. Astakhov, and V. Dyakonov, Excitation and coherent control of spin qudit modes in silicon carbide at room temperature, Nat. Commun. **10**, 1678 (2019).

[21] D. Simin, H. Kraus, A. Sperlich, T. Ohshima, G. V. Astakhov, and V. Dyakonov, Locking of electron spin coherence above 20 ms in natural silicon carbide, Phys. Rev. B **95**, 161201(R) (2017).

[22] T. Biktagirov, W. G. Schmidt, U. Gerstmann, B. Yavkin, S. Orlinskii, P. Baranov, V. Dyakonov, and V. Soltamov, Polytypism driven zero-field splitting of silicon vacancies in 6*H*-SiC, Phys. Rev. B **98**, 195204 (2018).

[23] Li-Ping Yang, C. Burk, M. Widmann, S.-Y. Lee, J. Wrachtrup, and N. Zhao, Electron spin decoherence in silicon carbide nuclear spin bath, Phys. Rev. B **90**, 241203(R) (2014).

[24] See Supplemental Material at http://link.aps.org/supplemental/10.1103/PhysRevB.103.195201 for the research results of the sample #3.

[25] H. Singh, A. N. Anisimov, S. S. Nagalyuk, E. N. Mokhov, P. G. Baranov, and D. Suter, Experimental characterization of spin-silicon vacancy centers in 6*H*-SiC, Phys. Rev. B **101**, 134110 (2020).

[26] H. De Raedt, B. Barbara, S. Miyashita, K. Michielsen, S. Bertaina, and S. Gambarelli, Quantum simulations and experiments on Rabi oscillations of spin qubits: Intrinsic vs extrinsic damping, Phys. Rev. B **85**, 014408 (2012).

[27] T. Yamamoto, T. Umeda, K. Watanabe, S. Onoda, M. L. Markham, D. J. Twitchen, B. Naydenov, L. P. McGuinness, T. Teraji, S. Koizumi, F. Dolde, H. Fedder, J. Honert, J. Wrachtrup, T. Ohshima, F. Jelezko, and J. Isoya, Extending spin coherence times of diamond qubits by high-temperature annealing, Phys. Rev. B **88**, 075206 (2013).

[28] S. Takahashi, R. Hanson, J. van Tol, M. S. Sherwin, and D. D. Awschalom, Quenching Spin Decoherence in Diamond through Spin Bath Polarization, Phys. Rev. Lett. **101**, 047601 (2008).

[29] C. Kasper, D. Klenkert, Z. Shang, D. Simin, A. Gottscholl, A. Sperlich, H. Kraus, C. Schneider, S. Zhou, M. Trupke, W. Kada, T. Ohshima, V. Dyakonov, and G. V. Astakhov, Influence of Irradiation on Defect Spin Coherence in Silicon Carbide, Phys. Rev. Appl. **13**, 044054 (2020).

[30] A. V. Duijn-Arnold, R. Zondervan, J. Schmidt, P. G. Baranov, and E. N. Mokhov, Electronic structure of the N donor center in 4*H*-SiC and 6*H*-SiC, Phys. Rev. B **64**, 085206 (2001).

[31] M. V. Muzafarova, I. V. Il'in, A. N. Anisimov, E. N. Mokhov, V. A. Soltamov, and P. G. Baranov, Electronic structure and spatial distribution of the spin density of shallow nitrogen donors in the SiC lattice, Phys. Solid State **58**, 2406 (2016).

[32] J. Schmidt and J. H. van der Waals, in *Time domain electron spin resonance*, edited by L. Kevan and R. N. Schwartz (Wiley, New York, 1979), p. 343.

[33] R. P. Feynman, F. L. Vernon, and R. W. Hellwarth, Geometrical representation of the Schrödinger equation for solving maser problems, J. Appl. Phys. **28**, 49 (1957).

[34] H. Singh, A. N. Anisimov, I. D. Breev, P. G. Baranov, and D. Suter, Optical spin initialization of spin-$\frac{3}{2}$ silicon vacancy centers in 6*H*-SiC at room temperature, Phys. Rev. B **103**, 104103 (2021).